Orthotropic organization of a cellulose nanocrystal suspension realized via the combined action of frontal ultrafiltration and ultrasound as revealed by in situ SAXS

Frédéric Pignon, Emilie Guilbert, Samuel Mandin, Nicolas Hengl, Mohamed Karrouch, Bruno Jean, Jean-Luc Putaux, Thomas Gibaud, Sebastien Manneville, Theyencheri Narayanan

Journal of Colloid and Interface Science xxx (xxxx) 1–12

Contents lists available at ScienceDirect

Journal of Colloid and Interface Science

journal homepage: www.elsevier.com

Regular Article

Orthotropic organization of a cellulose nanocrystal suspension realized via the combined action of frontal ultrafiltration and ultrasound as revealed by *in situ* SAXS

Frédéric Pignon [a, *], Emilie Guilbert [a], Samuel Mandin [a], Nicolas Hengl [a], Mohamed Karrouch [a], Bruno Jean [b], Jean-Luc Putaux [b], Thomas Gibaud [c], Sebastien Manneville [c, d], Theyencheri Narayanan [e]

[a] *Univ. Grenoble Alpes, CNRS, Grenoble INP (Institute of Engineering Univ. Grenoble Alpes), LRP, F-38000 Grenoble, France*
[b] *Univ. Grenoble Alpes, CNRS, CERMAV, F-38000 Grenoble, France*
[c] *ENSL, CNRS, Laboratoire de Physique, F-69342 Lyon, France*
[d] *Institut Universitaire de France, France*
[e] *ESRF - The European Synchrotron, F-38043 Grenoble, France*

ARTICLE INFO

Keywords:
Orthotropic
Cartilage
Liquid crystal
Cellulose nanocrystal
Ultrafiltration
Ultrasound
SAXS
Orientation
Structural organization

ABSTRACT

Hypothesis: Rodlike cellulose nanocrystals (CNCs) exhibit significant potential as building blocks for creating uniform, sustainable materials. However, a critical hurdle lies in the need to enhance existing or devise novel processing that provides improved control over the alignment and arrangement of CNCs across a wide spatial range. Specifically, the challenge is to achieve orthotropic organization in a single-step processing, which entails creating non-uniform CNC orientations to generate spatial variations in anisotropy.

Experiments: A novel processing method combining frontal ultrafiltration (FU) and ultrasound (US) has been developed. A dedicated channel-cell was designed to simultaneously generate (1) a vertical acoustic force thanks to a vibrating blade at the top and (2) a transmembrane pressure force at the bottom. Time-resolved *in situ* small-angle X-ray scattering permitted to probe the dynamical structural organization/orientation of CNCs during the processing.

Findings: For the first time, a typical three-layer orthotropic structure that resembles the articular cartilage organization was achieved in one step during the FU/US process: a first layer composed of CNCs having their director aligned parallel to the horizontal membrane surface, a second intermediate isotropic layer, and a third layer of CNCs with their director vertically oriented along the direction of US wave propagation direction.

1. Introduction

Cellulose nanocrystals (CNCs) are biosourced nanorods exhibiting a large variety of interesting intrinsic properties such as tunable aspect ratio and surface chemistry, exceptional mechanical properties, the ability to self-organize into liquid crystalline phases, non-toxicity, in addition to an abundant and renewable origin [1–5]. These particles can also be assembled into various types of controlled architectures using different processes (extrusion, coating, deposition, electrospinning, spin coating, bioprinting, etc.), yielding nanostructured cellulosic composites exhibiting a wide variety of functional properties [1–3,6–11]. For example, materials with specific optical (iridescence), mechanical (stiffness, anti-crack propagation) or barrier (oxygen or water) properties can be designed [12]. They could then impart a high-added value to materials in numerous applications such as microelectronics for pressure-sensitive screens [13], photonic films [14], in packaging for bio- and agroindustries [15], or in tissue engineering as stratified multilayered cartilage belonging to three-dimensional porous constructs [16–18].

Although CNCs have a high potential as elementary bricks in biosourced composites, achieving optimal performance of their functional properties is still difficult. One crucial challenge is to control the

Abbreviations: FU, frontal ultrafiltration; US, ultrasound; SAXS, small-angle X-ray scattering; CNC, cellulose nanocrystal; ESRF, European Synchrotron Radiation Facility; PCA, principal component analysis

* Corresponding author.
E-mail address: frederic.pignon@univ-grenoble-alpes.fr (F. Pignon).

https://doi.org/10.1016/j.jcis.2023.12.164
Received 3 October 2023; Received in revised form 21 December 2023; Accepted 28 December 2023
0021-9797/

orientation and organization of CNCs over a broad spatial scale. To achieve this goal, it is necessary to control, on the one hand, the interactions between CNCs and those between CNCs and their environment (e.g., aqueous or polymeric medium) and, on the other hand, the external forces induced by the processing. The control of internal interaction forces in aqueous CNC suspensions has been extensively studied in the past, both from the points of view of ionic control and their surface chemistry (adsorption or grafting) [19–21]. The effect of external solicitations on the structural organization of CNCs has also extensively been studied in the literature: for example, under shear flow [22–35], magnetic fields [36–40], electric fields [41], surface tension in drying processes [42–45], and solvation effect in solvent casting [46]. Recently, the ability of the ultrafiltration processes to induce well-defined layered structures of anisometric colloidal particles aligned horizontally along the velocity direction from nanometer to micrometer length scales has been demonstrated [47–54]. In addition, using ultrasound (US) waves, the control of the alignment of anisometric CNCs, with their director parallel to the direction of propagation of the ultrasonic wave, was revealed at an unprecedented nanometer scale [55]. However, to the best of our knowledge, no study has been reported on frontal ultrafiltration coupled with ultrasound to induce changes in the CNC orientation at micro to nanometer length scales.

In this work, we have used *in situ* time-resolved small-angle X-ray scattering (SAXS) to study the combined effects of frontal ultrafiltration (FU) and ultrasound (US) on the dynamical structural organization and orientation of CNCs in an aqueous medium, to develop orthotropic multilayered cellulosic structures with alternate perpendicular and parallel orientations as well as isotropic organization in each successive organized layer, reminiscent of the organization in the Strombus Gigas conch [56,57] and of articular cartilage [17,18,58]. In artificial or biological materials, such an orthotropic organization improves the stiffness and anti-crack propagation properties and confers high traction and compression resistance [59]. These properties can be reached by fulfilling two conditions: i) combining rigid and hard objects like nanocrystals with more flexible polymers, and ii) achieving a hierarchical structural organization over a broad range of length scales with an optimized distribution of crystalline particles in the organic matrix [60, 61]. For example, for shells submitted to a mechanical load, cracks do not propagate catastrophically through their crossed lamellar structure, increasing the work of fracture and hence the toughness of the material [57]. Another example is the complex hierarchical structure of articular cartilage tissue that is composed of three layers continuously structured from the articulating surface to the subchondral bone and extending over a total thickness of 2 to 4 mm. The first superficial region comprises a densely packed network of thin collagen fibers aligned parallel to the articular surface and extending from 10 to 20 % of the whole cartilage thickness. In the second middle transitional region, thicker collagen fibers are organized obliquely, giving rise to a random isotropic organization and corresponding to 40–60 % of the whole cartilage thickness. The third deep zone, composed of the largest collagen fibers perpendicular to the subchondral bone, takes up to 30 % of the entire cartilage thickness. These different layers have distinct mechanical properties imparted by their internal organization. Namely, the superficial zone has an optimized capability to dissipate shear forces, the middle transitional zone is the first line of resistance to compressive forces, and the deep zone has a high compression strength and interfacial resistance against shear forces [17,18,58].

To mimic this natural structural architecture and potentially reach comparable mechanical properties, a dedicated channel-type cell combining FU and US was developed (Fig. 1**)**. This cell was designed to simultaneously generate (i) a US pressure wave that induced a vertical acoustic radiation force, thanks to a vibrating ultrasonic blade inserted at the top of the channel and (ii) a transmembrane pressure force through a membrane designed for FU and located at the bottom of the channel. Importantly, to follow the structural organization within the cell upon the application of FU and US using small-angle X-ray scattering, it was implemented at the European Synchrotron Radiation Facility on the ID02 TRUSAXS beamline [62]. The structural organization of the CNC suspensions considered in this work has already been characterized in previous works [32,53,55,63]. The initial concentration of the suspension was fixed to C = 10 wt%, *i.e.* within the biphasic region of the phase diagram composed of isotropically distributed CNCs (isotropic phase) coexisting with the anisotropic chiral nematic (cholesteric) phase at a volume fraction of liquid crystalline phase ϕ_{LC} = 38 vol%.

Thanks to SAXS, the space and time dependence of the concentration of CNCs and their structural organization within the channel have been characterized as a function of the vertical distance z from the membrane surface to the ultrasonic blade, in the center of the 100 mm-long channel under combined ultrafiltration and ultrasound, hereafter referred to as FU-US processing. The 35-μm vertical size of the X-ray beam (full-width at half maximum, FWHM) allowed for accurate scans of the structural organization along the vertical direction during FU-US processing. The time-dependent evolution of the 2D SAXS patterns was analyzed using a model-free principal component analysis [64], which allowed us to describe both the degree of orientation and the direction of the alignment of the CNC director accurately as a function of z during FU-US processing in a time-resolved manner.

2. Experimental section

2.1. Materials. Preparation of the CNC suspensions

CNCs were purchased from UMaine Development Center (University of Maine, Orono, ME) as an aqueous suspension with a stock concentration C = 12.2 wt%. The suspensions were prepared by dilution in deionized water and 0.01 mol.L^{-1} NaCl, followed by 2 h of vigorous stirring. They were then sonicated using a Branson Digital sonifier (Marshall Scientific, Hampton, NH) with a maximum power output of 250 W. A volume of 250 mL of suspension was sonicated by applying a 30 % duty cycle and output power of 0.5 W.cm^{-2} under magnetic stirring. Following the procedure given by Taurozzi et al. [65], and the normalization by the concentration and volume of the suspension described in [66,67], the normalized energy dose of sonication per liter of suspension is 43.7 kJ.L^{-1}. The morphology of the CNCs considered in this work and their phase diagram in aqueous suspension have been studied in detail in previous work [63]. In particular, SAXS data from dilute suspensions at rest, assuming a parallelepipedal shape for the sonicated CNCs, gave average dimensions of 121 × 20 × 5 nm^3 [32, 53]. In this work, the concentration of CNC suspensions filtered was fixed at 10 wt% (6.25 vol%).

2.2. Experimental methods

2.2.1. Frontal ultrafiltration-ultrasound -SAXS cell

An FU-US-SAXS cell was developed to monitor *in situ* the changes in the dynamical structural organization through time-resolved SAXS [50, 68]. As shown in Fig. 1, the cell was made of transparent polycarbonate with a parallelepipedal channel with a 4 mm width along x, an 8 mm depth along z and a 100 mm length along y. A 3 mm-wide and 100 mm-long titanium vibrating blade was immersed from the upper part of the channel to a z distance = 5600 μm from the ultrafiltration membrane surface, defining the depth of the region where the suspension was structured by FU-US processing. In order to apply an acoustic radiation force along the vertical direction z, this blade was connected to a sonotrode (Sodeva TDS, Méry, France) consisting of a piezoelectric transducer attached to a metal rod, which generates ultrasonic waves at a frequency f_{US} = 20 kHz with an amplitude a_{US} [50,68,69]. This amplitude was measured to a_{US} = 1.6 μm using a vibrometry device consisting of a sensor head (OFV 353, Polytec, Waldbronn, Germany), a ve-

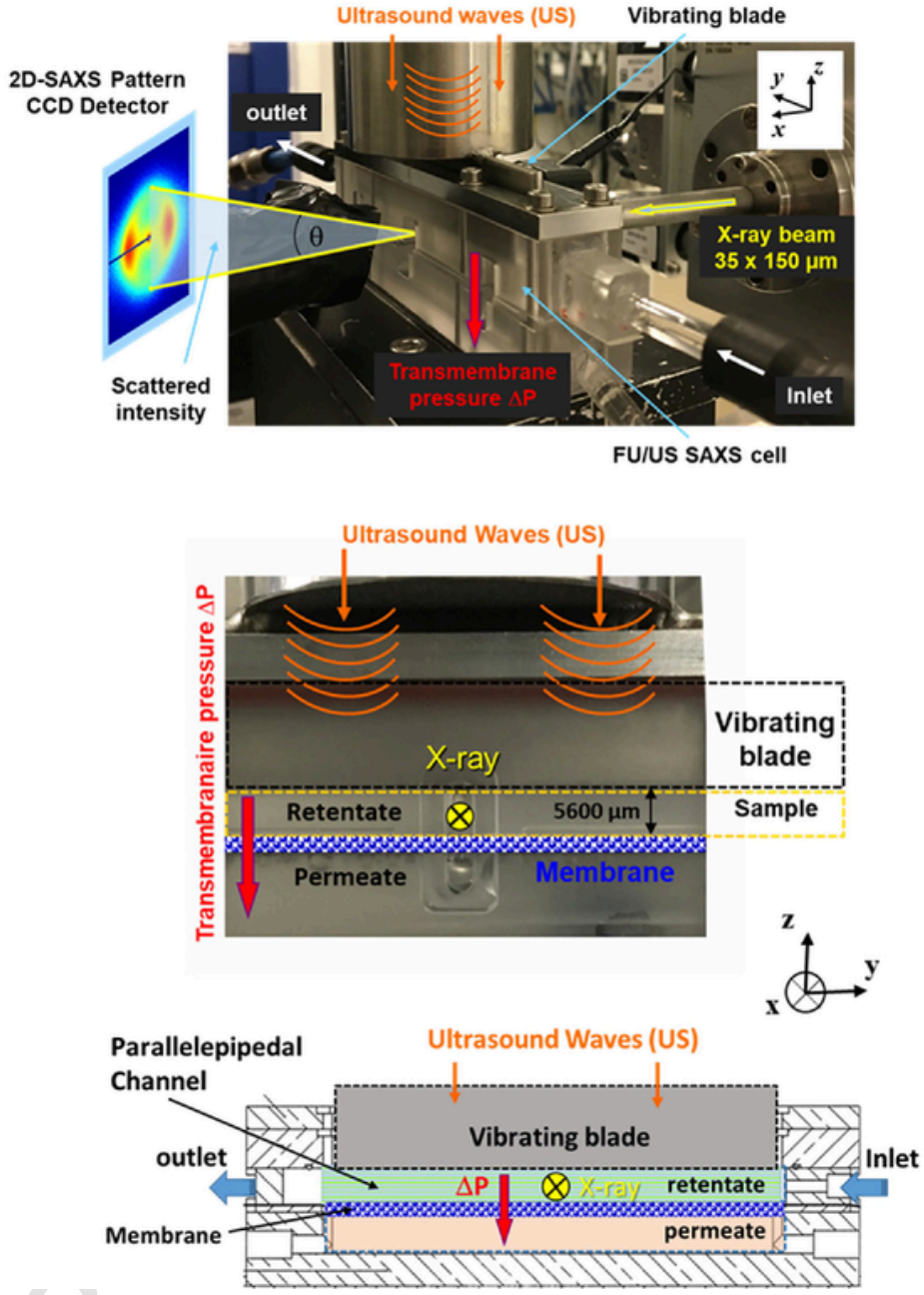

Fig. 1. Schematic description of the SAXS experiment with the dedicated FU-US-SAXS cell used to monitor the time-dependent changes of the structural organization of CNC suspensions under simultaneously applied transmembrane pressure and ultrasound waves.

locity decoder (OFV3001, Polytec) and an oscilloscope (DPO 3014, Tektronix, Beaverton, OR).

In order to apply the FU-US protocol described in more details below, the feed suspension, referred to as the retentate, was pumped with a syringe from a tank containing the CNC suspension and used to fill up the whole channel. An inlet vane and an outlet vane were positioned at the entrance and exit of the channel, respectively. A *T*-junction and a pressure gauge (FP 110 FGP Sensors & Instrument) were placed between the outlet vane and the outlet of the filtration cell. The upper part of the *T*-junction was connected to compressed air and the pressure vane was used to protect the air circuit from the suspension during the filling of the channel. The permeate was recovered in a small tank and the permeate flux J was monitored by measuring the mass variation of this tank reservoir every 10 s with an accuracy of 0.001 g using a precision scale (Precisa 400 M Balance).

2.2.2. In situ Small-Angle X-ray Scattering (SAXS) during FU-US processing.

SAXS measurements were performed at the TRUSAXS ID02 beamline (ESRF, Grenoble) [62]. Measurements were performed at room temperature with a sample-to-detector distance of 10 m and an X-ray energy of $E = 12.230$ keV (wavelength $\lambda = 0.1014$ nm), covering a range of scattering wave vector magnitude, q, of 0.005–0.7 nm^{-1}, where $q = (4\pi/\lambda)\sin(\theta/2)$ with θ the scattering angle. The corresponding nominal length scale l ($\sim 2\pi/q$) range was ca. 10 nm $\leq l \leq$ 1200 nm. Thanks to the pinhole collimation setup available at ID02, all the measurements were performed using a beam cross-section (FWHM) at the sample position of about 35 µm vertically and 150 µm horizontally. The incident beam passed through the sample in the FU-US-SAXS cell and the two-dimensional scattered intensity patterns were recorded on a high-resolution pixel array detector (Eiger2-4 M, Dectris) (Fig. 1). Mea-

sured scattering patterns were normalized to absolute scale following the standard procedure [62]. During the experiments, the X-ray beam was directed along the *x*-direction perpendicular to the walls of the cell, through a window of 3 mm × 5.5 mm × 0.3 mm (width × height × thickness) positioned in the middle of the channel (y = 50 mm). A rotational stage mounted on the sample table was used to align the incident beam parallel to the membrane surface. A vertical translation table was used to probe the structure at different z-positions above the membrane surface.

The analysis of the normalized SAXS patterns recorded in the FU-US-SAXS cell was the same as that already described in previous works [51,52,68,70]. Four regions were defined by measuring the transmitted X-ray signal as a function of the distance z through the FU-US-SAXS cell. This analysis has allowed defining the minimal distance z above which the permeate channel and membrane scattering did not influence the scattered intensity. We defined this z_0 position as the origin (z = 0). The minimal distance above which the SAXS data were usable was then z = 100 μm (determined by the planarity and roughness of the membrane). Systematic vertical scans along z were performed during FU-US processing, with SAXS pattern acquisitions every 50 μm from z = 100 to 500 μm and every 100 μm from z = 500 to 5600 μm. The one-dimensional scattered intensity profile $I(q)$ was obtained by azimuthally averaging the normalized scattering patterns. Before the FU-US experiments with CNC suspensions, the cell was filled with demineralized water and the normalized background scattering of the cell was recorded. This background scattering of the cell filled with water was systematically subtracted from the scattering of the CNC suspensions. The azimuthal averages of the scattering patterns were calculated after patching the gaps between the detector modules using the SAXSutilities software [71]. Annular averages were also calculated using the SAXSutilities software over a q-range from 0.34 to 0.40 nm^{-1} to define the scattering intensity as a function of the azimuthal scattering angle ψ in the plane of the two-dimensional 2D SAXS patterns to quantify the degree of orientation as well as its angular variation. The anisotropy analysis was performed from the 2D patterns using the MATLAB-based Small-Angle Scattering Evaluation Tool (SASET) software [64]. Specifically, the model-free Principal Component Analysis (PCA) method was chosen, which provides values for the anisotropy ranging from 0 for isotropic suspensions to 1 for fully aligned systems, and, depending on the system, which is quantitatively comparable to the commonly used order parameter [64]. The anisotropy and the direction of maximum scattering ψ_0 were calculated via PCA in the (0.071–0.368) nm^{-1} q-range. These calculations allowed us to quantify the relative effect of FU and US on the degree of anisotropy referred to as *PCA anisotropy* and on the orientation [maximum scattering direction (ψ_0)] of the CNCs during FU-US processing as a function of time t and distance z from the membrane surface.

2.2.3. Structure factor and calibration of cellulose nanocrystal scattering intensity.

In order to measure the CNC concentration profile as a function of filtration times and distance z from the membrane surface, the same analysis as described in our previous work has been applied [53]. First, a calibration curve was established. To this aim, several CNC samples at different known CNC concentrations were measured by SAXS in static conditions in a flow-through cell with a diameter of 2 mm. From the scattering intensities [$I(q)$] and the calculated form factor [$P(q)$] (**Fig. S1**) [53], the corresponding apparent structure factor, $S(q) \propto I(q)/P(q)$ was calculated for each known CNC concentration (Fig. 2 **a,b**). As previously discussed, in an effective hard-cylinder model (as an approximation of a repulsive potential), the q-value corresponding to the peak of $S(q)$, denoted as q_{peak} in the following, is related to the average interparticle distance d via the relation $d = 2\pi/q_{peak}$. Using this relationship, the known CNC concentration was related to the average interparticle distance d inferred from the peak of $S(q)$. As shown in Fig. 2c, a power-law fit of these data gave access to the relationship between the mass concentration C and d:

$$d = 84.08C^{-0.5} \text{ or, equivalently, } C = 8041d^{-2} \quad (1)$$

Second, from the scattered intensity $I(q)$ measured at a given position in the FU-US cell, the apparent structure factor, $S(q)$ was calculated at each time t and distance z from the membrane surface. From these $S(q)$ the corresponding average interparticle distances $d = 2\pi/q_{peak}$ at each time t and distance z from the membrane surface were evaluated. Finally, using Eq. (1), the corresponding local mass concentration $C(z,t)$ was calculated.

Another structural characteristic of these CNC suspensions is the organization in the cholesteric phase above a certain concentration threshold. Such a structural organization has been studied in detail at rest and under shear by small-angle light scattering in our previous works, which allowed measuring a pitch distance of about 5 μm at a concentration C = 10 wt% [32]. The helical pitch P corresponds to the distance needed for a 360° rotation of the director of one nanocrystal in the cholesteric phase, and P was reported to decrease with increasing concentration [24,32,72–74]. At the concentration studied here, the cholesteric phase exists as microdomains, or tactoids, distributed within the isotropic phase [75]. The volume fraction occupied by cholesteric tactoids at equilibrium was shown to be ϕ_{LC} = 38 vol% in the present suspension at C = 10 wt% [32,63].

2.2.4. Experimental protocol

The FU-US processing consisted of the following procedure. First, the cell was filled with the CNC suspension with an initial concentration C = 10 wt%. To this aim, the inlet and outlet valves were opened at the extremities of the channel, the pressure valve was closed, and the suspension was pumped from the tank with the syringe to fill up the whole channel. The inlet and outlet valves were then closed and the pressure valve was opened so that compressed air was injected from the T junction, allowing FU to start at time t = 0. Simultaneously, the US was activated.

For all the measurements presented in this work, only one acoustic radiation force was applied with a fixed acoustic amplitude a_{US} = 1.6 μm. This corresponded to an acoustic pressure $P = 2\pi\rho v f_{US} a_{US} \cong$ 300 kPa and an acoustic power $P_a = P^2/\rho v \cong$ 6 $W.cm^{-2}$, where ρ = 1000 $kg.m^{-3}$ is the water density and v = 1480 $m.s^{-1}$ is the speed of sound in water. No cavitation was observed. The transmembrane pressure was kept constant and equal to ΔP = 1.2 10^5 Pa. FU-US processing was applied for a total duration of 90 min. Meanwhile, the evolution of the 2D SAXS pattern was monitored and the corresponding permeation flux J was simultaneously recorded as a function of time t (Fig. 3). As displayed in Fig. 3, a few seconds after applying the transmembrane pressure ΔP, a rapid increase of the permeation flux J up to 20 $L.h^{-1}.m^{-2}$ was detected within about 1 s, followed by a steady decrease. After 30 min, J, reached an equilibrium at about 1 $L.h^{-1}.m^{-2}$, which is related to the well-known fouling phenomenon induced by the accumulation of CNCs near the membrane surface. As already reported in our previous works, the cellulose nanoparticles are retained at the membrane surface inducing a concentration gradient and a resistance to mass transfer [50–53].

3. Results and discussion

3.1. Cartilage-like structural organization at equilibrium under FU-US processing at time t = 88 min

The normalized *in situ* 2D SAXS patterns measured across the FU-US cell at time t = 88 min are shown in Fig. 4. The SAXS patterns are presented for distances z increasing from left to right and from bottom to top. For clarity, the corresponding z distances in micrometers are indicated in each 2D SAXS pattern. Remarkably, the intensity level and the

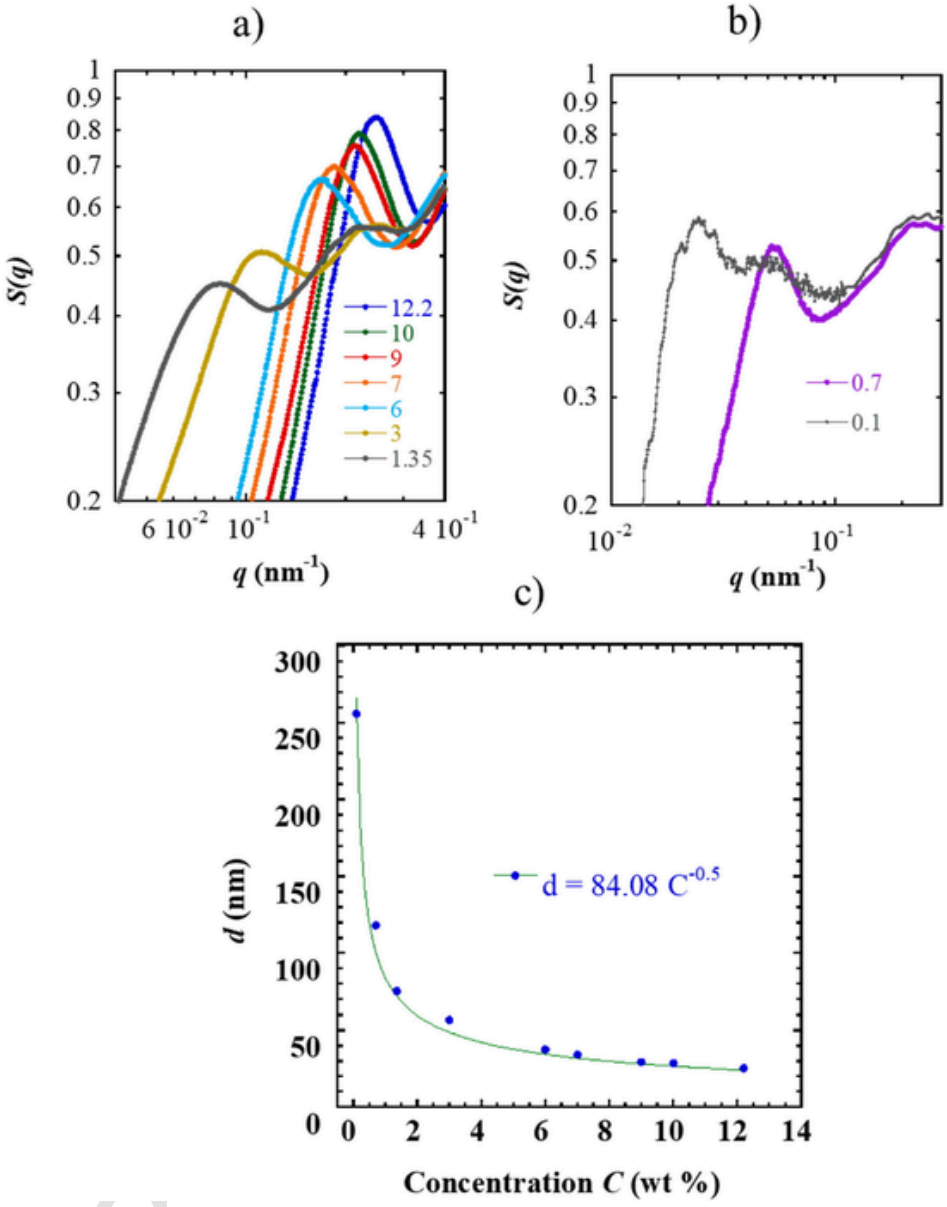

Fig. 2. a) and b) apparent structure factor, *S(q)* extracted from the calculated form factor and measured scattering intensity *I(q)*. The scale of *S(q)* may be slightly offset due to a mismatch between the calculated form factor and data at the high q region, where *S(q)* ~ 1. The values indicate the mass concentrations *C* (*i.e.*, in wt %) of aqueous CNC suspensions containing 0.01 mol.L^{-1} NaCl. c) Interparticle distance as a function of CNC concentration deduced from the q_{peak} q-value corresponding to the maximum of *S(q)*. The green line corresponds to an empirical power-law fit of the data (see Eq. (1)). From this calibration, it is possible to relate the peak of the calculated *S(q)* at a given distance *z* in the filtration cell to the average interparticle distance d, which can be used to estimate the corresponding mass concentration. (For interpretation of the references to color in this figure legend, the reader is referred to the web version of this article.)

orientation of the SAXS patterns strongly depended on the distance *z* from the membrane surface. Four regions, hereafter denoted as *Z1* to *Z4,* corresponding to different features of the 2D SAXS patterns in terms of direction degree of orientation of the CNCs have been identified.

(i) In the superficial region *Z1*, which extends from the membrane surface $z = 0$ until up to about $z = 1000$ μm, the pattern was anisotropic and elongated along the vertical direction. Under the effect of the transmembrane pressure, as previously observed [50–53], a regular orientation of the CNCs with their long axis parallel to the membrane surface (y-direction) is observed. (ii) In the second region *Z2* extending from $z = 1000$ to 1400 μm, the SAXS patterns evolved from slightly anisotropic, elongated along the vertical direction ($z = 1000$ μm), to perfectly isotropic ($z = 1200$ μm) and finally to slightly anisotropic, and elongated in the horizontal direction ($z = 1400$ μm). This intermediate region corresponds to a transition where the US and transmembrane pressure forces balance each other, which gives rise to an isotropic organization in the middle of this region. (iii) In the third region *Z3* extending from $z = 1400$ to 5000 μm, the SAXS patterns were elongated in the horizontal direction and revealed an orientation of the CNCs with their director vertically oriented along the direction of US wave propagation (*z*-direction), *i.e.,* oriented perpendicular to the membrane surface. In the *Z1*, *Z2*, and *Z3* regions, the SAXS patterns are stationary and only slightly fluctuated with time, showing a stabilization of the mean orientation direction of the CNCs, as confirmed in **Figure S2** in the middle of *Z3* region. (iv) In the fourth region *Z4* denoted as a *boundary layer* close to the surface of the US blade, which extends from $z = 5000$ to 5600 μm, significant fluctuations of the 2D SAXS patterns at short time scales, below 1 s, were observed (**Figure S3**).

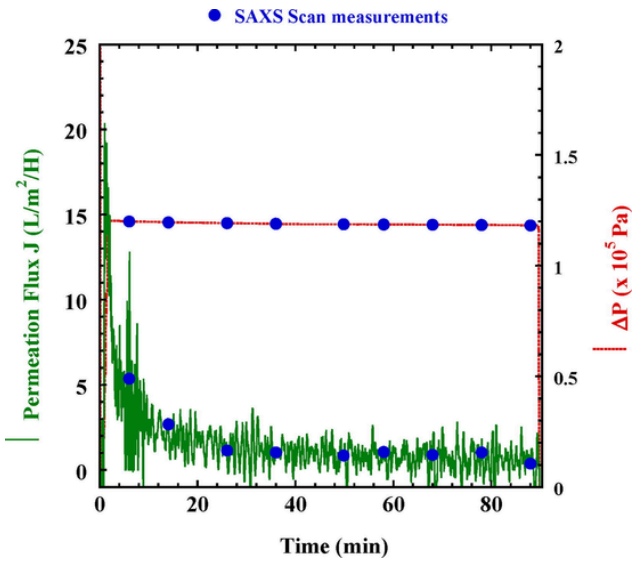

Fig. 3. Measured permeation flux J (green solid line) and applied transmembrane pressure ΔP (red dotted line) as a function of time t during FU-US processing of a CNC suspension with initial concentration C = 10 wt% and 0.01 mol.L^{-1} NaCl. The US parameters are f_{US} = 20 kHz, a_{US} = 1.6 μm, and $P \cong$ 300 kPa. The experiment was performed at room temperature. (For interpretation of the references to color in this figure legend, the reader is referred to the web version of this article.)

The azimuthally averaged *I(q),* and corresponding *S(q)* of the 2D SAXS patterns recorded at time t = 88 min in the channel as a function of the distance z from the membrane surface are plotted in Fig. 5. The general features of *I(q)* correspond well to the scattering of individualized CNCs at different concentrations, when compared to the scattering intensities of CNC suspensions at a fixed concentration measured in a capillary (Fig. 2). In particular, *S(q)* (Fig. 5b) exhibits a maximum at a specific q-value, q_{peak}, which reveals a well-defined average interparticle distance d, as in Fig. 2. This allowed us to confirm that the CNCs were well distributed without being broken down or aggregated under the effect of FU-US processing.

For each z position, the determination of q_{peak} from *S(q)* allowed us to calculate the concentration level reached in the different layers using **Eq. (1)**. The first accessible point measured closest to the membrane surface and calculated from the structure factor (z = 150 μm), corresponds to an interparticle distance d = 11.7 nm, and a CNC mass fraction of C = 59 wt%. From z = 150 to 1200 μm, the peak position q_{peak} strongly shifted to lower q-values, which implies a substantial decrease of the concentration across the superficial region, as shown in Fig. 6 (see filled blue symbols), *i.e.*, a pronounced vertical concentration gradient. This effect corresponds to the concentration polarization layer in membrane ultrafiltration processes [50–52,68]. This deposit layer extends from z = 150 μm with C = 59 wt% to z = 1200 μm with C = 16 wt%, as depicted in Figs. 5 and 6.

Above z = 1200 μm and up to the surface of the US blade at z = 5600 μm, the peak position q_{Peak} remains unchanged and yields an interparticle distance d = 22.6 nm, corresponding to a uniform C = 16 wt% concentration. It is worth noting that this concentration is significantly larger than the concentration C = 10 wt% of the initial suspension, which shows that the FU-US process allowed us not only to concentrate the CNCs near the membrane surface as in a usual filtration process but also to concentrate the suspension in the whole bulk of the retentate, by the effect of US. The latter phenomenon is certainly due to a permeation flux enhanced by the local agitation induced by the US force, as discussed in previous works [50,68].

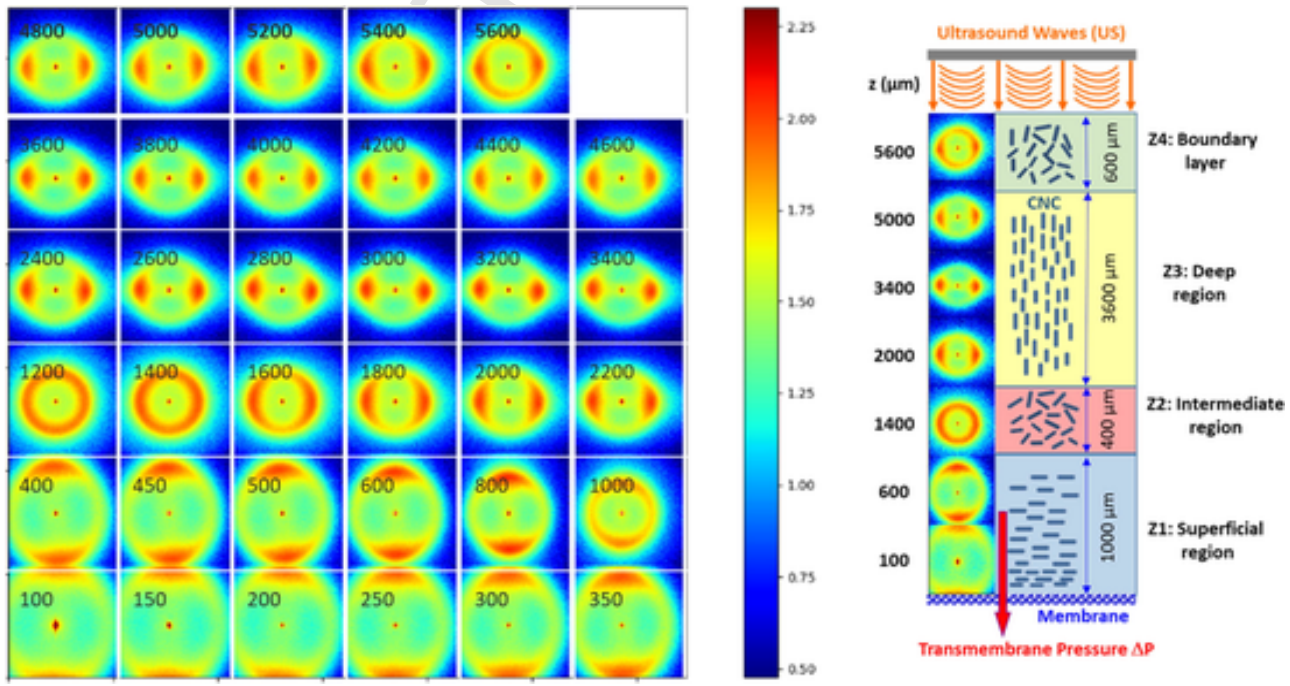

Fig. 4. Left: 2D SAXS patterns recorded as a function of the distance z from the membrane surface at time t = 88 min of the FU-US processing of a CNC suspension with initial concentration C = 10 wt% and 0.01 mol.L^{-1} NaCl. The US parameters were f_{US} = 20 kHz, a_{US} = 1.6 μm, and $P \cong$ 300 kPa, and the transmembrane pressure was $\Delta P = 1.2 \times 10^5$ Pa. The distance z = 5600 μm corresponds to the vicinity of the surface of the US blade. Right: sketch of the four regions pertaining to the SAXS pattern features from bottom to top of the channel: the first three regions noted *Z1*, *Z2*, and *Z3* are the superficial, intermediate, and deep regions, respectively, and mimic the typical orthotropic organization of articular cartilage. These regions are stable in orientation over time. Region *Z4* (boundary layer) near the US blade surface, exhibits a fluctuating intensity of the orientation on a time scale below 1 s.

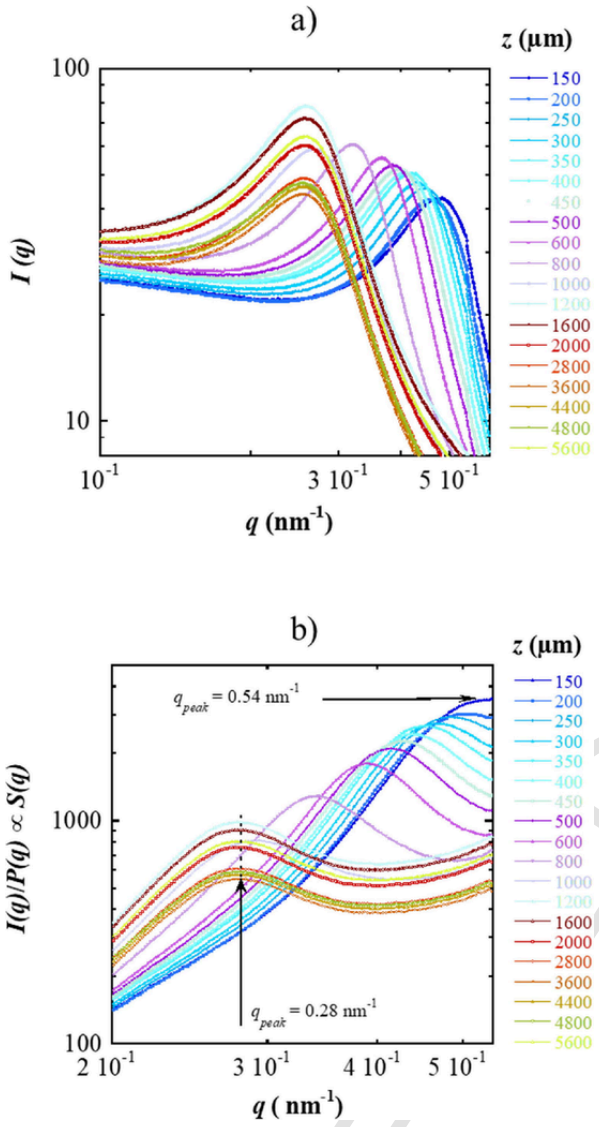

Fig. 5. a) azimuthally averaged scattering intensities $I(q)$ and b) corresponding apparent structure factor, $S(q)$ of the 2D saxs patterns recorded at time t = 88 min under FU-US processing and different positions z from the membrane surface in a CNC suspension with initial concentration C = 10 wt% and 0.01 mol.L^{-1} NaCl. The color code corresponds to the position z. ΔP = 1.2 × 10^5 Pa, f_{US} = 20 kHz, and a_{US} = 1.6 µm.

The very high concentration C = 59 wt% reached near the membrane surface, as well as the homogeneous increase from the initial concentration C = 10 wt% up to a constant value of C = 16 wt% from z = 1200 to 5600 µm, show the ability of the FU-US process to concentrate the colloidal suspension. This new structuring process could be an excellent way to design highly concentrated CNC-based materials. Indeed, other processes allowing for such a concentration level, e.g., high-speed centrifugation or osmotic pressure, would require processing times longer than the 90 min FU-US processing used in this work.

3.2. Time evolution of the structural organization under FU-US processing (concentration and orientation features)

In order to describe more quantitatively the structural organization achieved under FU-US processing, we systematically performed a Principal Component Analysis of the anisotropy (*PCA anisotropy*) and determined the direction of maximum scattering ψ_0 on the 2D SAXS patterns as a function of position z and time t [53,64]. Furthermore, the evolution of the azimuthally averaged scattering intensity and the corresponding calculated structure factors $S(q)$ have also been analyzed near the membrane surface to deduce the concentration profile as a function of position z and time t.

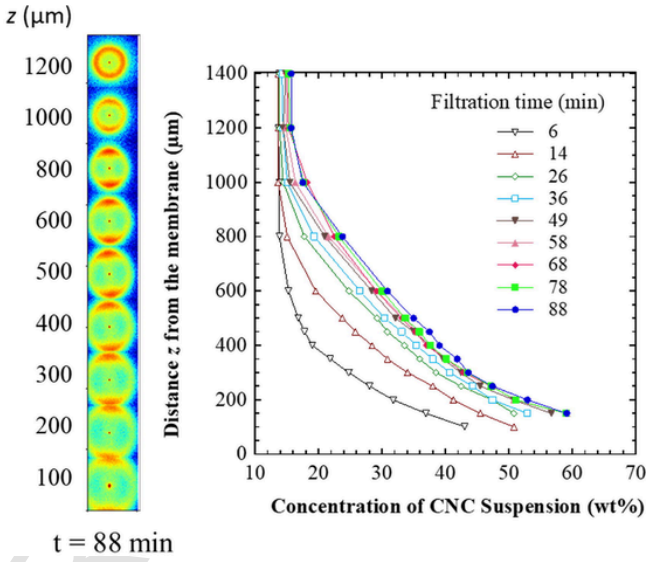

Fig. 6. Concentration profile $C(z,t)$ in the superficial region $Z1$ as a function of the distance z from the membrane surface and for various times t during FU-US processing of a CNC suspension with initial concentration C = 10 wt% and 0.01 mol.L^{-1} NaCl. The concentration is deduced from the corresponding 2D SAXS pattern, the estimated $S(q)$, and the calibration curve using **Eq.** (1). ΔP = 1.2 × 10^5 Pa, f_{US} = 20 kHz, and a_{US} = 1.6 µm.

3.2.1. Time evolution of the CNC concentration near the membrane surface in the superficial region Z1

Fig. 6 displays the time evolution of the concentration profiles C (z, t) computed from the characteristic q_{peak} value of the corresponding $S(q)$ calculated from azimuthally averaged SAXS patterns using **Eq.** (1). After t = 6 min of FU-US processing, an impressive 800 µm-thick concentrated layer, reaching a concentration of about 43 wt% at z = 100 µm, was already formed. Such a high concentration, reached within a rather short frontal ultrafiltration time under US, is most likely related to the huge decrease of the permeation flux J from 20 to 1 L.h^{-1}.m^{-2} (Fig. 3). In particular, as already discussed in previous studies [50,68], it could be associated with an effect of the agitation near the membrane surface induced by the US acoustic radiation force. After this initial deposition, the superficial layer increased in thickness and concentration, until reaching a constant thickness of about 1200 µm after 36 min. This increase in deposit volume is due to the pressure gradient, which leads to the advection of the CNCs from the less concentrated layers far away from the membrane toward deeper concentrated layers in the direction of the membrane. This suggests that, in the presence of US, the concentration phenomenon is not an accumulation of independent layers, as in a sedimentation process, but rather results from the advection of all the particles from the top of the deposit towards the membrane surface. During the whole FU-US processing, the concentration at the top of the superficial region continuously increased from the initial concentration C = 10 wt% up to 16 wt%, yet without reaching a complete steady state. This phenomenon is expected from frontal ultrafiltration, since the filtration is performed from an initial fixed volume without any further suspension feeding. Indeed, the volume of water (permeate) that goes through the membrane implies an increase in the concentration in the retentate. Still, the increase of the total concentration in the retentate channel gets slower and slower due to slower advection as the concentration increases. This allowed us to define a pseudo-steady state, for which the

time-dependent concentration and orientation phenomena were mostly stabilized at t = 88 min (see next section).

3.2.2. Time evolution of the anisotropy and orientation degree of CNCs from the membrane to the US blade

Fig. 7 shows the time evolutions of the *PCA anisotropy* and of the direction of maximum scattering ψ_0 as a function of z for the four regions *Z1* to *Z4* identified and described previously.

To further investigate this time-dependent process, radial averages were calculated over a q-range from 0.34 to 0.40 nm^{-1} to define the scattering intensity I as a function of the azimuthal scattering angle ψ in the plane of the 2D SAXS patterns in order to quantify the degree of orientation as well as its angular variation.

3.2.2.1. Superficial region Z1 of anisotropic concentrated polarized layer. A surprising phenomenon was detected in the superficial region *Z1* corresponding to the concentration polarization layer near the membrane surface. According to our previous works on the same CNC system [51–53], an increase in concentration toward the membrane was related to a continuous rise in anisotropy: the more concentrated the system, the higher the degree of anisotropy. Here, however, we report a non-monotonic evolution of the *PCA anisotropy* across region *Z1*: as depicted in Fig. 8, the *PCA anisotropy* goes through a maximum at a particular distance z that depends on the FU-US processing time. This "bifurcation" point is located at larger distances from the membrane surfaces as the processing time increases, which is consistent with a thicker and thicker concentrated polarization layer. The progression of this effect is as follows: from z = 1200 μm distance down to the membrane surface at z = 0, the anisotropy first increases, and follows the increase of concentration, which is consistent with our previous works [51–53] until the "bifurcation" point, where the anisotropy starts to decrease down to the membrane surface. Another way to check for such a process in the opposite direction, *i.e.*, looking from the membrane surface towards increasing z distances, is presented in **Figure S4**, where the annular averages of scattering intensities were calculated over a q-range from 0.34 to 0.40 nm^{-1} at time t = 88 min. The results confirmed the anisotropy increase for increasing distances z from the membrane surface until the "bifurcation" point at z = 800 μm for this particular processing time. Above z = 800 μm, the anisotropy decreased with increasing distances z from the membrane surface, until the scattering intensity $I(\psi)$ showed a nearly flat profile at z = 1200 μm (**Figure S5**).

The usual increase of anisotropy at increasing concentration is induced by a nematic-like arrangement of the CNCs with all their directors aligned along the horizontal direction and mostly around the same angular direction in the (x,y) plane. Scanning electron microscopy (SEM) images of deposits have confirmed such an arrangement after drying in the two perpendicular planes (x,y) and (x,z) [53].

One possible explanation for the decrease of the anisotropy below the "bifurcation" point towards the membrane surface would be the presence of a cholesteric organization in the layers close to the membrane. Indeed, in such a cholesteric arrangement, the CNC director would continuously change in direction in the (x,y) plane while describing the helix of the cholesteric organization oriented with its helical axis along the z-axis. The pitch of these chiral nematic CNC suspensions is known to be of the order of a few micrometers (around 5 μm at C = 10 wt%, and lower for higher concentrations) [32]. Since the extent of the X-ray beam in the vertical direction is collimated to 35 μm (FHWM), and considering that the helix axes are mostly aligned along the vertical direction, the scattering intensity recorded at a position z would thus be representative of an average of the director orientations over several pitches, (in agreement with the horizontal orientation of

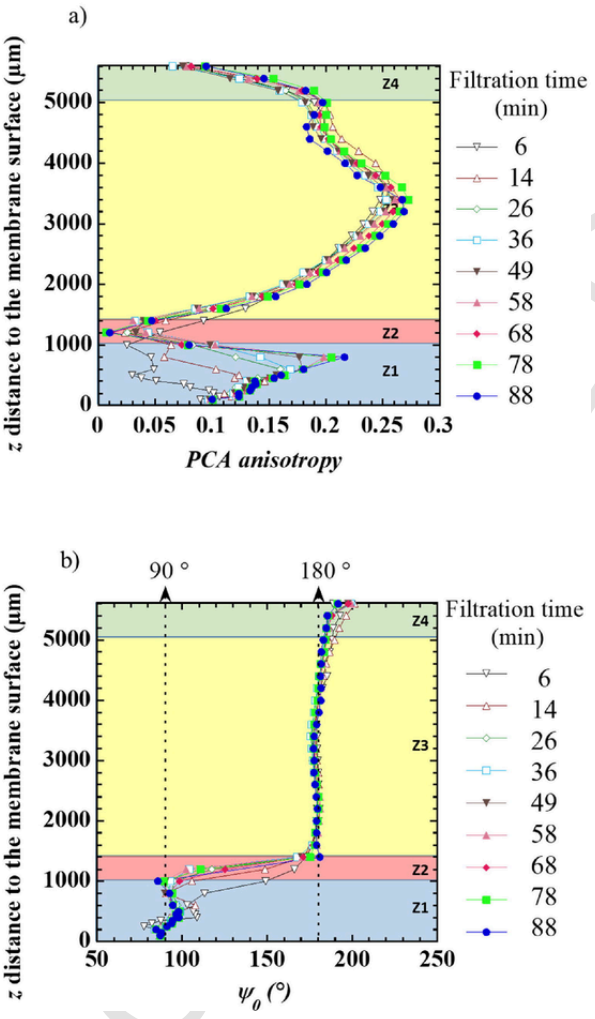

Fig. 7. a) PCA anisotropy and b) direction of maximum scattering ψ_0 as a function of the distance z and from the membrane surface and for various times t during FU-US processing, inferred from the Principal Component Analysis of the 2D SAXS patterns in the superficial region *Z1* (blue), the intermediate region *Z2* (red), the deep region *Z3* (yellow) and the boundary layer *Z4* (green). ψ_0 = 90° corresponds to an orientation of the CNCs along the horizontal direction x, while ψ_0 = 180° corresponds to an orientation of the CNCs along the vertical direction z. CNC suspension with initial concentration C = 10 wt% and 0.01 mol.L^{-1} NaCl. ΔP = 1.2 × 10^5 Pa, f_{US} = 20 kHz, and a_{US} = 1.6 μm. (For interpretation of the references to color in this figure legend, the reader is referred to the web version of this article.)

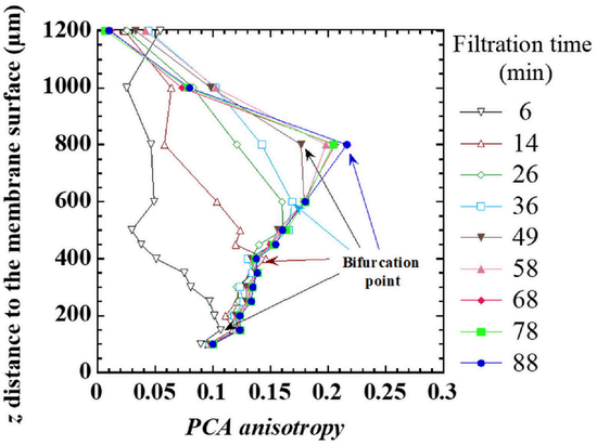

Fig. 8. Enlargement of the PCA anisotropy as a function of z and at various processing times t. Same data as in Fig. 7a in the superficial region Z1.

the CNC director, confirmed by the mean value of maximum scattering direction ψ_0 around 90° from $z = 0$ to 1200 μm, see Fig. 7b.

This continuous variation of the CNC director orientation in the volume probed by the X-ray beam induces a decrease of the anisotropy, compared to the situation where a nematic-like arrangement is present with a single mean CNC director orientation in the (*x,y*) plane. Considering the high concentrations reached in these layers, one can infer that the structural organization goes from the nematic arrangement usually observed in these accumulated layers in the presence of shear forces to a cholesteric organization above a particular concentration [42,47–49]. Under the combined transmembrane pressure and US acoustic radiation force, it is very likely that this concentration limit evolves towards concentrations larger than the limit of appearance of the cholesteric organization in the equilibrium phase diagram ($C_i \sim 7.5$ wt%) and larger than the second critical concentration corresponding to the onset of the fully anisotropic cholesteric phase ($C_a \sim 13.3$ wt%). Indeed, the interparticle forces responsible for the cholesteric formation would compete with the shearing forces induced by the flow of liquid around the CNC generated by the permeation flux and the US agitation. Consequently, a larger concentration is probably mandatory to nucleate a cholesteric arrangement under FU-US processing. Future work should also check whether tactoids form first and whether their continuous increase in volume fraction finally results in a complete cholesteric organization as in equilibrium conditions. One could also wonder whether the transition mechanism from nematic to cholesteric arrangement follows the same concentration range under FU-US processing as in equilibrium conditions, or as upon cessation of a high shear flow [31].

Another feature supporting this hypothesis of a progressively stronger cholesteric organization in the polarization layer is that for increasing processing times, the "bifurcation" point appears at larger and larger distances from the membrane surface and that the maximum *PCA anisotropy* at this "bifurcation" point increases linearly with the distance from the bifurcation point to the membrane surface (Fig. 8). This supports the fact that when the formation of a cholesteric arrangement is reached at the "bifurcation" point, an increase of concentration towards the membrane induces more and more cholesteric arrangements, *i.e.*, an increase of the volume fraction of the cholesteric arrangement relative to the nematic-like order. This would decrease the global orientation of the CNC director along a common direction, leading to the reduction of the *PCA anisotropy* towards the membrane surface.

3.2.2.2. Intermediate region Z2 of isotropic orientation. In the intermediate layer from $z = 1000$ to 1400 μm, the *PCA anisotropy* remained low and showed a minimum for $z \sim 1200$ μm, *i.e.*, in the middle of region *Z2* (Fig. 7a). Concomitantly, the direction of maximum scattering ψ_0 evolved from 90 to 180° (Fig. 7b). The annular average of the scattering intensity confirms this reversal of orientation from $z = 800$ to 1400 μm with a decrease of anisotropy until $z = 1200$ μm (nearly flat profile) followed by an increase of anisotropy at larger z distances (**Figure S5**).

3.2.2.3. Deep region Z3 of anisotropic orientation. As shown in Fig. 7a, in region *Z3*, the *PCA anisotropy* steadily increased from its lowest level at $z = 1200$ μm until reaching a maximum value of 0.28 at $z = 3600$ μm and further decreasing weakly towards the vibrating blade up to $z = 5000$ μm, where another "bifurcation" signals the transition to the fourth region *Z4*. The corresponding annular average of the scattering intensity shows that the anisotropy indeed increases at the beginning of region *Z3* (**Figure S6**) and then decreases from $z = 3600$ to 5000 μm at the top of region *Z3* (**Figure S7**). The anisotropy in region *Z3* corresponds to a well-oriented SAXS pattern elongated in the horizontal direction as confirmed by the value of $\psi_0 \cong 180°$, which confirms the vertical orientation of the CNC director in the deep region.

3.2.2.4. Boundary layer region Z4 of decreasing anisotropic orientation near the US blade. In the fourth region *Z4* extending from $z = 5000$ to 5600 μm, both the anisotropy and the orientation of the 2D SAXS patterns fluctuate over a characteristic time scale below 1 s (**Figure S4**). This induces a decrease in the *PCA anisotropy* from about 0.2 to about 0.1, which is confirmed by the change in the amplitude and shape of the annular averaged scattering intensity (**Figure S7**).

Finally, it is worth noticing that the *PCA anisotropy* and the angle ψ_0 follow similar time evolutions throughout regions *Z2*, *Z3*, and *Z4* (Fig. 7), which implies that the complex structuration induced by transmembrane pressure in region *Z1* does not significantly alter the effect of US in the upper regions, where the US acoustic force drives the orientation of CNCs.

3.3. Origin of the orientation of CNCs induced by the US acoustic radiation force

As discussed in our previous work [55], the question of the physical origin of the orientation of colloidal objects or molecules induced by US force has been addressed by several authors. The main mechanisms have been summarized by Vitoriano [76]. Two mechanisms have been proposed. For the first mechanism, the molecular orientation could result from acoustic streaming arising from convective stresses. The second mechanism is of elastic nature and linked to the anisotropy of sound absorption by liquid crystals, which, according to Prigogin's principle, must lead to the alignment of long nematic molecules in the direction of acoustic wave propagation [76]. From our initial analysis using the same US equipment yet in the absence of FU [55], the most probable explanation is that the first mechanism of acoustic streaming would induce the CNC orientation under US agitation.

The argument in favor of this hypothesis is that the time-dependent evolution of anisotropy relaxation after cessation of US is of the order of a few minutes and follows a stretched exponential behavior associated with a complex structural change, involving several mechanisms, which does not agree with the second mechanism associated to a faster elastic process induced by the anisotropy of sound absorption.

Another argument in favor of this explanation based on the first mechanism of acoustic streaming comes from the fluctuation of anisotropy detected near the surface of the US blade. In particular, it is well known that the US vibration induces the presence of a region with steady vorticity in a viscous boundary layer of thickness $\delta_v = (2\nu/\omega)^{0.5}$ close to the vibrating surface, where ν is the kinematic viscosity and ω the angular frequency of the acoustic wave. Such an "inner boundary layer streaming", also known as "Schlichting streaming", goes along with a counter-rotating streaming vortex within the bulk of the fluid, referred to as "outer boundary layer streaming" or "Rayleigh streaming" [77]. The theory implies that the appearance of the Rayleigh streaming phenomenon requires specific boundary conditions and confined flow, similar to the ones in our system. More precisely, Schlichting or Rayleigh streaming is promoted when $\lambda_a \gg h \gg \delta_v$, where λ_a is the acoustic wavelength and h is the characteristic length scale of the fluid chamber [77]. For our experimental setup, these conditions are indeed satisfied since ($\lambda_a = 7.5$ cm) $\gg h =$ (3800 μm to 5600 μm) $\gg \delta_v =$ (40 to 126 μm) when taking into account the range of variation of the viscosity of the CNC suspension ($\nu = 10^{-3}$ to 10^{-4} Pa.s). Furthermore, Tang and Hu [78] have performed finite-element simulations of the acoustic streaming field generated in a 2D rectangular water chamber by a vibrating source. An operating frequency of 20 kHz with amplitude of 100 nm, *i.e.*, the same frequency as in the present work yet with an amplitude about 16 times lower than the amplitude $a_{US} = 1.6$ μm of our device. The simulations by Tang and Hu [78] revealed that the acoustic streaming field is constituted of two kinds of vortices: (i) vortices distributed symmetrically on the right and left of the vibration source and confined near the vibrating source, *i.e.*, within the inner boundary layer vorticity, and (ii) counter-rotating streaming vortices

within the bulk of the chamber corresponding to Rayleigh streaming vortices. Considering the fluctuation of anisotropy detected near the surface of the US blade (**Figure S4**), one can infer that the corresponding region *Z4* should pertain to the inner boundary layer, where a fast rotation of the CNC director is expected in agreement with the fluctuations of anisotropy observed in region *Z4*. We may also hypothesize that Rayleigh streaming vortices are developed in the bulk of the cell, so that the corresponding streamlines induce an alignment of the CNCs along the velocity field, *i.e.*, along the vertical direction, in agreement with the preferential vertical orientation observed in region *Z3*.

Therefore, all the features discussed here suggest that Rayleigh streaming constitutes the physical origin of the orientation of CNCs induced by the US waves. Nevertheless, deeper investigations would be helpful to fully assess this hypothesis, such as *in situ* measurements of the velocity field during FU-US processing. This could be achieved by means of particle image velocimetry (PIV).

4. Conclusions

An original combined frontal ultrafiltration (FU) and ultrasound (US) set-up compatible with *in situ* SAXS observations has allowed to reveal for the first time a multilayer orthotropic structuring of CNC suspensions, that mimics the organization of articular cartilage. Thanks to model-free principal component analysis and annular averaged scattering intensities, we have accurately described both the degree of orientation and the direction of the alignment of the CNC director in the bulk of the channel, from the membrane surface up to the US blade during FU-US processing in a time-resolved manner.

We have interpreted our observations, in particular the length scales and time scales involved in the spectacular alignment of the CNCs along the ultrasonic wave propagation direction in terms of Rayleigh acoustic streaming initiated by the viscous attenuation of the acoustic waves generated by the vibrating blade. This interpretation remains to be fully confirmed. *In situ* micro-PIV measurements could be a good way to assess the validity of the Rayleigh streaming scenario in future work. Finally, the successful control over the average orientation of CNCs by combined FU and US opens a new way for the design of novel cellulosic orthotropic biomimetic materials with tunable structural organization for tissue engineering applications.

CRediT authorship contribution statement

Frédéric Pignon: Writing – review & editing, Writing – original draft, Validation, Supervision, Project administration, Methodology, Investigation, Formal analysis. **Emilie Guilbert:** Writing – review & editing, Investigation, Formal analysis. **Samuel Mandin:** Writing – review & editing, Investigation, Formal analysis. **Nicolas Hengl:** Writing – review & editing, Investigation, Formal analysis. **Mohamed Karrouch:** Investigation. **Bruno Jean:** Writing – review & editing, Investigation, Formal analysis. **Jean-Luc Putaux:** Writing – review & editing, Investigation, Formal analysis. **Thomas Gibaud:** Writing – review & editing, Investigation, Formal analysis. **Sebastien Manneville:** Writing – review & editing, Investigation, Formal analysis. **Theyencheri Narayanan:** Writing – review & editing, Investigation, Formal analysis.

Declaration of competing interest

The authors declare that they have no known competing financial interests or personal relationships that could have appeared to influence the work reported in this paper.

Data availability

Data will be made available on request.

Acknowledgment

We thank Jacques Gorini (ESRF, Grenoble), Didier Blésès, Frédéric Hugenell and Eric Faivre (Laboratoire Rhéologie et Procédés) for technical assistance. ESRF is acknowledged for provision of synchrotron beamtime (proposal SC-5110). The author(s) acknowledge(s) the support of the French Agence Nationale de la Recherche (ANR), under grant ANR-20-CE43-0015 (ANISOFILM) and of the Région Auvergne-Rhône-Alpes "Pack Ambition Recherche" Programme. LRP is part of LabEx Tec21 (Investissements d'Avenir - grant agreement #ANR-11-LABX-0030). LRP and CERMAV are part of Institut Carnot PolyNat (Investissements d'Avenir - grant agreement #ANR-16-CARN-0025-01), and the Glyco@Alps programme (Investissements d'Avenir - grant agreement #ANR-15-IDEX-02).

Appendix A. Supplementary data

Supplementary data to this article can be found online at https://doi.org/10.1016/j.jcis.2023.12.164.

References

[1] G. Siqueira, J. Bras, A. Dufresne, Cellulosic bionanocomposites: a review of preparation, properties and applications, Polymers 2 (2010) 728–765, https://doi.org/10.3390/polym2040728.

[2] B. Thomas, M.C. Raj, K.B. Athira, M.H. Rubiyah, J. Joy, A. Moores, G.L. Drisko, C. Sanchez, Nanocellulose, a versatile green platform: from biosources to materials and their applications, Chem. Rev. 118 (2018) 11575–11625, https://doi.org/10.1021/acs.chemrev.7b00627.

[3] C. Schütz, J.R. Bruckner, C. Honorato-Rios, Z. Tosheva, M. Anyfantakis, J.P.F. Lagerwall, From equilibrium liquid crystal formation and kinetic arrest to photonic bandgap films using suspensions of cellulose nanocrystals, Crystals 10 (2020) 199, https://doi.org/10.3390/cryst10030199.

[4] D. Trache, A.F. Tarchoun, M. Derradji, T.S. Hamidon, N. Masruchin, N. Brosse, M.H. Hussin, Nanocellulose From fundamentals to advanced application, Front. Chem. 8 (2020) 392, https://doi.org/10.3389/fchem.2020.00392.

[5] C. Tom, S.N. Sangitra, R.K. Pujala, Rheological fingerprinting and applications of cellulose nanocrystal based composites: A review, J. Mol. Liq. 370 (2023) 121011, https://doi.org/10.1016/j.molliq.2022.121011.

[6] J.P.F. Lagerwall, C. Schütz, M. Salajkova, J. Noh, J.H. Park, G. Scalia, L. Bergstrom, Cellulose nanocrystal-based materials: from liquid crystal self-assembly and glass formation to multifunctional thin films, Npg Asia Materials 6 (2014) e80.

[7] A. Tang, J. Li, J. Li, S. Zhao, W. Liu, T. Liu, J. Wang, Y.A. Liu, Nanocellulose/PEGDA aerogel scaffolds with tunable modulus prepared by stereolithography for three-dimensional cell culture, Biomater. Sci. Polym. 30 (2019) 797–814, https://doi.org/10.1038/am.2013.69.

[8] M. Schwartz, G. Lenzini, Y. Geng, P.B. Rønne, P.Y.A. Ryan, J.P.F. Lagerwall, Cholesteric liquid crystal shells as enabling material for information-rich design and architecture, Adv. Mater. 30 (2018) 1707382, https://doi.org/10.1002/adma.201707382.

[9] B.A. Frost, B.P. Sutliff, P. Thayer, M.J. Bortner, E.J. Foster, Gradient poly [ethylene glycol] diacrylate and cellulose nanocrystals tissue engineering composite scaffolds via extrusion bioprinting, Front. Bioeng. Biotechnol. 7 (280) (2019) 1–14, https://doi.org/10.3389/fbioe.2019.00280.

[10] O. Kose, C.E. Boott, W.Y. Hamad, M.J. MacLachlan, Stimuli-responsive anisotropic materials based on unidirectional organization of cellulose nanocrystals in an elastomer, Macromolecules 52 (14) (2019) 5317–5324, https://doi.org/10.1021/acs.macromol.9b00863.

[11] K.J. De France, Z. Zeng, T. Wu, G. Nyström, Functional materials from nanocellulose: Utilizing structure–property relationships in bottom-up fabrication, Adv. Mater. 33 (2021), https://doi.org/10.1002/adma.202000657.

[12] A. Dufresne, Nanocellulose: From Nature to High Performance Tailored Materials, second ed., Walter de Gruyter GmbH, Berlin/Boston, 2017. Doi: 10.1515/9783110254600.

[13] M. Mitov, Chlolesteric liquid crystals in living matter, Soft Matter 13 (2017) 4176–4209, https://doi.org/10.1039/C7SM00384F.

[14] B. Frka-Petesic, B. Guidetti, G. Kamita, S. Silvia Vignolini, Controlling the photonic properties of cholesteric cellulose nanocrystal films with magnets, Adv. Mater. 29 (2017) 1606208, https://doi.org/10.1002/adma.201701469.

[15] H. Kargarzadeh, J. Huang, N. Lin, I. Ahmad, M. Mariano, A. Dufresne, S. Thomas, A. Galeski, Recent developments in nanocellulose-based biodegradable polymers, thermoplastic polymers, and porous nanocomposites, Prog. Polym. Sci. 87 (2018) 197–227, https://doi.org/10.1016/j.progpolymsci.2018.07.008.

[16] R.M.A. Domingues, M.E. Gomes, R.L. Rei, The potential of cellulose nanocrystals in tissue engineering strategies, Biomacromolecules 15 (2014) 2327–2346, https://doi.org/10.1021/bm500524s.

[17] S. Camarero-Espinosa, J. Cooper-White, Tailoring biomaterial scaffolds for osteochondral repair, Int. J. Pharm. 523 (2) (2017) 476–489, https://doi.org/10.1016/j.ijpharm.2016.10.035.

[18] N. Khuu, S. Kheiri, E. Kumacheva, Structurally anisotropic hydrogels for tissue engineering, Trends Chem. 3 (12) (2021) 1002–1026, https://doi.org/10.1016/j.trechm.2021.09.009.

[19] F. Azzam, L. Heux, J.-L. Putaux, B. Jean, Preparation by grafting onto, characterization, and properties of thermally responsive polymer-decorated cellulose nanocrystals, Biomacromolecules 11 (2010) 3652–3659, https://doi.org/10.1021/bm101106c.

[20] F. Azzam, E. Siqueira, S. Fort, R. Hassaini, F. Pignon, C. Travelet, J.-L. Putaux, B. Jean, Tunable aggregation and gelation of thermoresponsive suspensions of polymer-grafted cellulose nanocrystals, Biomacromolecules 17 (2016) 2112–2119, https://doi.org/10.1021/acs.biomac.6b00344.

[21] E. Gicquel, C. Martin, L. Heux, B. Jean, J. Bras, Adsorption versus grafting of poly [N-Isopropylacrylamide] in aqueous conditions on the surface of cellulose nanocrystals, Carbohydr. Polym. 210 (2019) 100–109, https://doi.org/10.1016/j.carbpol.2019.01.022.

[22] W.J. Orts, L. Godbout, R.H. Marchessault, J.-F. Revol, Enhanced ordering of liquid crystalline suspensions of cellulose microfibrils: A small angle neutron scattering study, Macromolecules 31 (1998) 5717–5725, https://doi.org/10.1021/ma9711452.

[23] T. Ebeling, M. Paillet, R. Borsali, O. Diat, A. Dufresne, J.-Y. Cavaillé, H. Chanzy, Shear-induced orientation phenomena in suspensions of cellulose microcrystals, revealed by small angle X-ray scattering, Langmuir 15 (1999) 6123–6126, https://doi.org/10.1021/LA990046%2B.

[24] S. Shafiei-Sabet, W.Y. Hamad, S.G. Hatzikiriakos, Rheology of nanocrystalline cellulose aqueous suspensions, Langmuir 28 (2012) 17124–17133, https://doi.org/10.1021/la303380v.

[25] B. Derakhshandeh, G. Petekidis, S. Shafiei-Sabet, W.Y. Hamad, S.G. Hatzikiriakos, Ageing, yielding, and rheology of nanocrystalline cellulose suspensions, J. Rheol. 57 (2013) 131–148, https://doi.org/10.1122/1.4764080.

[26] A.D. Haywood, K.M. Weigandt, P. Saha, M. Noor, M.J. Green, V.A. Davis, New insights into the flow and microstructural relaxation behavior of biphasic cellulose nanocrystal dispersions from RheoSANS, Soft Matter 13 (2017) 8451–8462, https://doi.org/10.1039/C7SM00685C.

[27] Y. Xu, A.D. Atrens, J.R. Stokes, Rheology and microstructure of aqueous suspensions of nanocrystalline cellulose rods, J. Colloid Interface Sci. 496 (2017) 130–140, https://doi.org/10.1016/j.jcis.2017.02.020.

[28] Y. Xu, A. Atrens, J.R. Stokes, A review of nanocrystalline cellulose suspensions: Rheology, liquid crystal ordering and colloidal phase behaviour, Adv. Colloid Interface Sci. 275 (2020) 102076, https://doi.org/10.1016/j.cis.2019.102076.

[29] L. Sanchez-Botero, A.V. Dimov, R. Li, D.-M. Smilgies, J.O. Hinestroza, In situ and real-time studies, via synchrotron X-ray scattering, of the orientational order of cellulose nanocrystals during solution shearing, Langmuir 34 (2018) 5263–5272, https://doi.org/10.1021/acs.langmuir.7b04403.

[30] W. Qi, J. Yu, Z. Zhang, H.-N. Xu, Effect of pH on the aggregation behavior of cellulose nanocrystals in aqueous medium, Mater. Res. Express 6 (2019) 125078, https://doi.org/10.1088/2053-1591/ab5974.

[31] T. Rosén, R. Wang, C. Zhan, H. He, S. Chodankar, S. Benjamin, B.S. Hsiao, Cellulose nanofibrils and nanocrystals in confined flow: Single-particle dynamics to collective alignment revealed through scanning small-angle x-ray scattering and numerical simulations, Phys. Rev. E 101 (2020) 032610, https://doi.org/10.1103/PhysRevE.101.032610.

[32] F. Pignon, M. Challamel, A. De Geyer, M. Elchamaa, E.F. Semeraro, N. Hengl, B. Jean, J.L. Putaux, E. Gicquel, J. Bras, S. Prevost, M. Sztucki, T. Narayanan, H. Djeridi, Breakdown and buildup mechanisms of cellulose nanocrystal suspensions under shear and upon relaxation probed by SAXS and SALS, Carbohydr. Polym. 260 (2021) 117751, https://doi.org/10.1016/j.carbpol.2021.117751.

[33] R. Kádár, S. Stefan Spirk, T. Nypelö, Cellulose nanocrystal liquid crystal phases: Progress and challenges in characterization using rheology coupled to optics, scattering, and spectroscopy, ACS Nano 15 (2021) 7931–7945, https://doi.org/10.1021/acsnano.0c09829.

[34] V. Calabrese, S.J. Haward, A.Q. Shen, Effects of shearing and extensional flows on the alignment of colloidal rods, Macromolecules 54 (9) (2021) 4176–4185, https://doi.org/10.1021/acs.macromol.0c02155.

[35] K. Håkansson, A. Fall, F. Lundell, et al., Hydrodynamic alignment and assembly of nanofibrils resulting in strong cellulose filaments, Nat. Commun. 5 (2014) 4018, https://doi.org/10.1038/ncomms5018.

[36] J. Sugiyama, H. Chanzy, G. Maret, Orientation of cellulose microcrystals by strong magnetic fields, Macromolecules 25 (1992) 4232–4234, https://doi.org/10.1021/ma00042a032.

[37] B. Frka-Petesic, J. Sugiyama, S. Kimura, H. Chanzy, G. Maret, Negative diamagnetic anisotropy and birefringence of cellulose nanocrystals, Macromolecules 48 (2015) 8844–8857, https://doi.org/10.1021/acs.macromol.5b02201.

[38] K.J. De France, K.G. Yager, T. Hoare, E.D. Cranston, Cooperative ordering and kinetics of cellulose nanocrystal alignment in a magnetic field, Langmuir 32 (2016) 7564–7571, https://doi.org/10.1021/acs.langmuir.6b01827.

[39] R.M. Parker, B. Frka-Petesic, G. Guidetti, G. Kamita, G. Consani, C. Abell, S. Vignolini, Hierarchical self-assembly of cellulose nanocrystals in a confined geometry, ACS Nano 10 (9) (2016) 8443–8449, https://doi.org/10.1021/acsnano.6b03355.

[40] T. Chen, Q. Zhao, X. Meng, Y. Li, H. Peng, A.K. Whittaker, S. Zhu, Ultrasensitive magnetic tuning of optical properties of films of cholesteric cellulose nanocrystals, ACS Nano 14 (8) (2020) 9440–9448, https://doi.org/10.1021/acsnano.0c00506.

[41] B. Frka-Petesic, H. Radavidson, B. Jean, L. Heux, Dynamically controlled iridescence of cholesteric cellulose nanocrystal suspensions using electric fields, Adv. Mater. 29 (2017) 1606208, https://doi.org/10.1002/adma.201606208.

[42] V. Cherpak, V.F. Korolovych, R. Geryak, T. Turiv, D. Nepal, J. Kelly, T.J. Bunning, O.D. Lavrentovich, W.T. Heller, V.V. Tsukruk, Robust chiral organization of cellulose nanocrystals in capillary confinement, Nano Lett. 18 (11) (2018) 6770–6777, https://doi.org/10.1021/acs.nanolett.8b02522.

[43] A. Tran, W.Y. Hamad, M.J. MacLachlan, Fabrication of cellulose nanocrystal films through differential evaporation for patterned coatings, ACS Appl. Nano Mater. 1 (2018) 3098–3104, https://doi.org/10.1021/acsanm.8b00947.

[44] D.G. Gray, X. Mu, Twist–bend stage in the relaxation of sheared chiral nematic suspensions of cellulose nanocrystals, ACS Omega 1 (2016) 212–219, https://doi.org/10.1021/acsomega.6b00100.

[45] C. Bruel, S. Queffeulou, P.J. Carreau, J.R. Tavares, M.-C. Heuzey, Orienting cellulose nanocrystal functionalities tunes the wettability of water-cast films, Langmuir 36 (2020) 12179–12189, https://doi.org/10.1021/acs.langmuir.0c01799.

[46] C. Bruel, T.S. Davies, P.J. Carreau, J.R. Tavares, M.C. Heuzey, Self-assembly behaviors of colloidal cellulose nanocrystals: A tale of stabilization mechanisms, J. Colloid Interface Sci. 574 (2020) 399–409, https://doi.org/10.1016/j.jcis.2020.04.049.

[47] Q. Chen, P. Liu, F. Nan, L. Zhou, J. Zhang, Tuning the iridescence of chiral nematic cellulose nanocrystal films with a vacuum-assisted self-assembly technique, Biomacromolecules 15 (11) (2014) 4343–4350, https://doi.org/10.1021/bm501355x.

[48] Z. Wang, N. Li, L. Zong, J. Zhang, Recent advances in vacuum assisted self-assembly of cellulose nanocrystals, Curr. Opin. Solid State Mater. Sci. 23 (2019) 142–148, https://doi.org/10.1016/j.cossms.2019.03.001.

[49] Z. Wang, Y. Yuan, J. Hu, J. Yang, F. Feng, Y. Yu, P. Liu, Y. Men, J. Zhang, Origin of vacuum-assisted chiral self-assembly of cellulose nanocrystals, Carbohydr. Polym. 245 (2020) 116459, https://doi.org/10.1016/j.carbpol.2020.116459.

[50] Y. Jin, N. Hengl, S. Baup, F. Pignon, N. Gondrexon, M. Sztucki, A. Romdhane, A. Guillet, M. Aurousseau, Ultrasonic assisted cross-flow ultrafiltration of starch and cellulose nanocrystals suspensions: Characterization at multi-scales, Carbohydr. Polym. 124 (2015) 66–76, https://doi.org/10.1016/j.carbpol.2015.01.073.

[51] C. Rey, N. Hengl, S. Baup, M. Karrouch, E. Gicquel, A. Dufresne, H. Djeridi, R. Dattani, Y. Jin, F. Pignon, Structure, rheological behavior and in situ local flow-fields of cellulose nanocrystal dispersions during cross-flow ultrafiltration, ACS Sustain. Chem. Eng. 7 (2019) 10679–10689, https://doi.org/10.1021/acssuschemeng.9b01333.

[52] C. Rey, N. Hengl, S. Baup, M. Karrouch, A. Dufresne, H. Djeridi, R. Dattani, F. Pignon, Velocity, stress and concentration fields revealed by micro-PIV and SAXS within concentration polarization layers during cross-flow ultrafiltration of colloidal laponite clay suspensions, J. Membr. Sci. 578 (2019) 69–84, https://doi.org/10.1016/j.memsci.2019.02.019.

[53] E.F. Semeraro, N. Hengl, M. Karrouch, L.J. Michot, E. Paineau, B. Jean, J.-L. Putaux, C. Lancelon-Pin, L. Sharpnack, F. Pignon, Layered organization of anisometric cellulose nanocrystals and beidellite clay particles accumulated near the membrane surface during cross-flow ultrafiltration: In situ SAXS and ex situ SEM/WAXD characterization, Colloids Surf. A 584 (2020) 124030, https://doi.org/10.1016/j.colsurfa.2019.124030.

[54] C. Kocaman, E. Bukusoglu, P.Z. Culfaz-Emecen, Correction to controlling ultrafiltration membrane rejection via shear-aligned deposition of cellulose nanocrystals from aqueous suspensions, ACS Appl. Mater. Interfaces 14 (20) (2022) 24071, https://doi.org/10.1021/acsami.2c07509.

[55] F. Pignon, E.F. Semeraro, W. Chèvremont, H. Bodiguel, N. Hengl, M. Karrouch, M. Sztucki, Orientation of cellulose nanocrystals controlled in perpendicular directions by combined shear flow and ultrasound waves studied by small-angle x-ray scattering, J. Phys. Chem. C 125 (2021) 18409–18419, https://doi.org/10.1021/acs.jpcc.1c03506.

[56] A.Y.M. Lin, M.A. Meyers, K.S. Vecchio, Mechanical properties and structure of Strombus gigas, Tridacna gigas, and Haliotis rufescens sea shells: A comparative study, Mater. Sci. Eng. C 26 (2006) 1380–1389, https://doi.org/10.1016/j.msec.2005.08.016.

[57] S. Kamat, X. Su, R. Ballarini, A.H. Heuer, Structural basis for the fracture thoughness of the shell of the conch Strombus gigas, Nature 405 (2000) 1036–1040, https://doi.org/10.1038/35016535.

[58] A.J. Sophia Fox, A. Bedi, S.A. Rodeo, The basic science of articular cartilage: Structure, composition, and function, Sports Health 1 (6) (2009) 461–468, https://doi.org/10.1177/1941738109350438.

[59] Y. Shin, S. Yin, X. Li, et al., Nanotwin-governed toughening mechanism in hierarchically structured biological materials, Nat. Commun 7 (2016) 10772, https://doi.org/10.1038/ncomms10772.

[60] L. Chen, R. Ballarini, H. Kahn, A.H. Heuer, Bioinspired micro-composite structure, J. Mater. Res. 22 (1) (2007) 124–131, https://doi.org/10.1557/jmr.2007.0016.

[61] K. Bertoldi, D. Bigoni, W.J. Drugan, Nacre An orthotropic and bimodular elastic material, Compos. Sci. Technol. 68 (2008) 1363–1375, https://doi.org/10.1016/j.compscitech.2007.11.016.

[62] T. Narayanan, M. Sztucki, T. Zinn, J. Kieffer, A. Homs-Puron, J. Gorini, P. Van Vaerenbergh, P. Boesecke, Performance of the time-resolved ultra-small-angle X-ray scattering beamline with the Extremely Brilliant Source, J. Appl. Crystallogr. 55 (2022) 98–111, https://doi.org/10.1107/s1600576721012693.

[63] E. Gicquel, J. Bras, C. Rey, J.-L. Putaux, F. Pignon, B. Jean, C. Martin, Impact of sonication on the rheological and colloidal properties of highly concentrated cellulose nanocrystal suspensions, Cellulose 26 (2019) 7619–7634, https://doi.org/10.1007/s10570-019-02622-7.

[64] M. Muthig, S. Prévost, R. Orglmeister, M. Gradzielski, SASET: A program for series analysis of small-angle scattering data, J. Appl. Crystal. 46 (2013) 1187–1195, https://doi.org/10.1107/S0021889813016658.

[65] J.S. Taurozzi, V.A. Hackley, M.R. Wiesner, Ultrasonic dispersion of nanoparticles for environmental, health and safety assessment – issues and recommendations, Nanotoxicology 5 (4) (2011) 711–729, https://doi.org/10.3109/17435390.2010.528846.

[66] M. Girard, D. Vidal, F. Bertrand, J.R. Tavares, M.C. Heuzey, Evidence-based guidelines for the ultrasonic dispersion of cellulose nanocrystals, Ultrasonics Sonochemistry 71 (2021) 105378, https://doi.org/10.1016/j.ultsonch.2020.105378.

[67] M.A. Johns, C. Lam, B. Zakani, et al., Comparison of cellulose nanocrystal dispersion in aqueous suspension via new and established analytical techniques, Cellulose 30 (2023) 8259–8274, https://doi.org/10.1007/s10570-023-05348-9.

[68] Y. Jin, N. Hengl, S. Baup, F. Pignon, N. Gondrexon, A. Magnin, M. Sztucki, T. Narayanan, L.J. Michot, B. Cabane, Effects of ultrasound on colloidal organization at nanometer length scale during cross-flow ultrafiltration probed by in situ SAXS, J. Membr. Sci. 453 (2014) 624–635, https://doi.org/10.1016/j.memsci.2013.12.001.

[69] T. Gibaud, N. Dagès, P. Lidon, G. Jung, L.C. Ahouré, M. Sztucki, A. Poulesquen, N. Hengl, F. Pignon, S. Manneville, Rheoacoustic gels: tuning mechanical and flow properties of colloidal gels with ultrasonic vibrations, Phys. Rev. X 10 (2020) 011028, https://doi.org/10.1103/PhysRevX.10.011028.

[70] F. Pignon, M. Abyan, C. David, A. Magnin, M. Sztucki, In situ characterization by SAXS of concentration polarization layers during cross-flow ultrafiltration of Laponite dispersions, Langmuir 28 (2012) 1083–1094, https://doi.org/10.1021/la201492z.

[71] M. Sztucki, SAXSutilities: a graphical user interface for processing and analysis of Small-Angle X-ray Scattering data [1.024], 2021, doi: 10.5281/zenodo.5825707.

[72] X.M. Dong, T. Kimura, J.-F. Revol, D.G. Gray, Effects of ionic strength on the isotropic–chiral nematic phase transition of suspensions of cellulose crystallites, Langmuir 12 (1996) 2076–2082, https://doi.org/10.1021/la950133b.

[73] J.-F. Revol, H. Bradford, J. Giasson, R.H. Marchessault, D.G. Gray, Helicoidal self-ordering of cellulose microfibrils in aqueous suspension, Int. J. Biol. Macromol. 14 (1992) 170–172, https://doi.org/10.1016/s0141-8130(05)80008-x.

[74] E.E. Ureña-Benavides, G. Ao, V.A. Davis, C.L. Kitchens, Rheology and phase behavior of lyotropic cellulose nanocrystal suspensions, Macromolecules 44 (2011) 8990–8998, https://doi.org/10.1021/ma201649f.

[75] P. Wang, W. Hamad, M. MacLachlan, Structure and transformation of tactoids in cellulose nanocrystal suspensions, Nat. Commun. 7 (2016) 11515, https://doi.org/10.1038/ncomms11515.

[76] C. Vitoriano, Acousto-optic effect in nematic liquid crystals: Experimental evidence of an elastic regime, Phys. Rev. E 88 (2013) 032501, https://doi.org/10.1103/PhysRevE.88.032501.

[77] M. Wiklund, R. Green, M. Ohlin, Acoustofluidics 14: Applications of acoustic streaming in microfluidic devices, Lab Chip 12 (2012) 2438–2451, https://doi.org/10.1039/C2LC40203C.

[78] I. Tang, J. Hu, Diversity of acoustic streaming in a rectangular acoustofluidic field, Ultrasonics 58 (2015) 27–34, https://doi.org/10.1016/j.ultras.2014.11.015.